Research Article Vol. 33, No. 3 / 10 Feb 2025 / Optics Express 3901
Optics EXPRESS

Toward low-noise on-chip plasmonic three-dimensional biological cell imaging

MALIHA MOMTAJ AND MUHAMMAD ANISUZZAMAN TALUKDER*

Department of Electrical and Electronic Engineering, Bangladesh University of Engineering and Technology, Dhaka 1205, Bangladesh
*anis@eee.buet.ac.bd

Abstract: Enhancing accessibility to affordable and efficient cell imaging tools has been a longstanding worldwide objective for rapid disease detection and diagnosis. We present an innovative approach to this goal, introducing a compact, portable, and user-friendly three-dimensional (3D) cell imaging platform leveraging silicon photonics and the surface plasmon coupled emission (SPCE) phenomenon. Central to our method is a specially designed slide that incorporates a fundamental SPCE structure seamlessly integrated with a silicon nitride (SiN) waveguide. We introduce a grooved array on the slide to couple light into the waveguide, interfacing with a broadband light source. This source is employed to excite fluorescently labeled cells. The excitation is achieved using edge coupling through the SiN waveguide, directing the excitation light to the specimen placed on the SPCE platform. This integrated architecture eliminates the necessity for an additional filter to extract the required light for fluorophore excitation while enabling precise excitation of labeled cells. Following the fluorophore excitation, the emitted SPCE signals are captured and subjected to analysis. We have developed an imaging algorithm based on the emitted light patterns, which we comprehensively detail through theoretical demonstration. This algorithm has the remarkable capability of achieving 3D cell imaging. This fusion of optics and computational techniques can significantly impact the domain of cell imaging by enabling the development of easily accessible and portable point-of-care (POC) imaging tools.

1. Introduction

Cell imaging provides crucial information about the physical properties of cells affected by infectious diseases. Cell imaging is particularly valuable in diagnosing and treating diseases like cancer, cranial nerve disorders, thyroid diseases, lipomas, and tumors [1–3]. Recent studies have highlighted the significance of physical changes in blood cells in the context of COVID-19, emphasizing the potential of cell imaging in understanding and diagnosing the disease [4–6]. However, current clinical imaging techniques, such as X-ray, computed tomography (CT), magnetic resonance imaging (MRI), single-photon emission computerized tomography (SPECT), positron emission tomography (PET), and ultrasounds, have limitations like low spatial resolution, lengthy acquisition times, high expenses, radiation exposure, and bulky equipment [1,7,8]. These constraints hinder real-time in vivo analysis of biological and cellular events. Additionally, the scarcity and unequal distribution of qualified health human resources in many regions, especially rural areas, further hinder accessibility to advanced healthcare technologies [9]. The development of low-cost POC bioimaging instruments has become imperative to improve healthcare accessibility and overcome the challenges posed by traditional clinical imaging techniques [10]. Such POC imaging tools can significantly reduce manual labor and result in turnaround time, making diagnostics more efficient and timelier, especially in resource-poor settings [11,12].

Optical imaging techniques are advantageous for designing POC medical diagnostic devices. They offer real-time, high-resolution imaging techniques at microscopic and macroscopic levels, enabling fast and precise diagnoses [10]. Advancements in optoelectronics, optical fibers,

#546204 https://doi.org/10.1364/OE.546204
Journal © 2025 Received 25 Oct 2024; revised 10 Dec 2024; accepted 17 Dec 2024; published 27 Jan 2025

Optics EXPRESS

optical microelectromechanical systems (MEMS), and micro-optics have led to smaller and more cost-effective optical imaging platforms [13]. Several optical imaging methods, including conventional light microscopes, confocal laser scanning microscopes (CLSM) [14], optical sectioning structured illumination microscopes (OS-SIM) [15,16], and light sheet fluorescence microscopes (LSFM) [17], direct optical nanoscopy with axially localized detection (DONALD) [18], have been developed to provide compact and well-integrated imaging modalities for POC applications. Nevertheless, imaging three-dimensional (3D) specimens using these optical sectioning methods remains challenging. The sequential recording of images plane by plane may lead to phototoxic damage and photobleaching [19], impacting the accuracy of results. Additionally, effectively managing the substantial amount of data ("big data") for 3D imaging is a concern. Therefore, the need for on-chip imaging modalities supported by efficient computational algorithms arises alongside the miniaturization and integration of optical imaging platforms.

In contrast to conventional optical imaging techniques, fluorescence-based imaging technology stands out for its exceptional spatial and temporal resolution, rapid data processing, and widespread accessibility [20,21]. Recently, a surface-enhanced fluorescence technique known as SPCE has garnered significant attention in bioimaging. This technique offers a range of attractive features, including greater sensitivity, distinctive axial confinement, and efficient background suppression [22]. Particularly noteworthy is its highly directional emission, which enhances collection efficiency and detection sensitivity [23]. The angular dependence and wavelength resolution properties of SPCE hold the potential for enhancing imaging selectivity [24]. SPCE reduces photodamage during observation [22], making it well-suited for capturing cellular structures and dynamics. In addition, SPCE instrumentation does not require bulky hardware, leading to the implementation of low-cost and portable SPCE-based imaging techniques [25]. Despite these advancements, most SPCE-based imaging systems provide only two-dimensional (2D) views of cellular structures. While promising 3D cell imaging techniques have been introduced [26], their focus has primarily been on algorithmic development, leaving the operational framework of the imaging system unaddressed. However, understanding the system's functionality as a whole is essential for its practical implementation in biomedical research.

Against this backdrop, this work introduces an innovative SPCE-based 3D cell imaging platform with minimalist optics. By integrating existing optomechanical (wavelength selection devices like monochromators or filters) components onto a single slide, we effectively overcome the limitations of conventional techniques, offering a compact, cost-effective, and potent solution for POC cell imaging. The slide serves as a stable platform for holding samples while interfacing with the light sources and detectors. It consists of a simple SPCE structure integrated with a grooved array. This array acts as a precise wavelength filter, enabling the selective excitation of fluorescently labeled cells. We selected rhodamine B as the fluorescent dye because it is widely used for studying cells. The strategic design of the grooved structure ensures optimal light coupling, ~53% of the incident light, at the desired wavelength. When interfaced with a broadband light source, this grooved configuration produces narrowband light. Furthermore, it can efficiently couple light from a smartphone flashlight, allowing for a compact system design. A waveguide coupled to this grating structure effectively directs this light toward the fluorescently labeled cells on the SPCE structure side atop a glass spacer layer. When illuminated by this narrowband light, the labeled cell undergoes excitation, causing the fluorophores within the specimen to emit fluorescent light, which then creates SPCE through a thin metal layer. The SPCE originates from surface-confined light, effectively reducing background noise from out-of-focus light in our imaging system.

Finally, we have developed an algorithm for label-based cell imaging. This algorithm analyzes and processes the emitted fluorescent light from the labeled cell. The algorithm aims to determine the coordinates (x, y, z) of fluorophores located on the cell surface. With these coordinates, we successfully recreate the 3D structure of the cell with a root mean square error (RMSE) of <

Optics EXPRESS

2.7%. To verify the effectiveness of our approach, we rigorously calculate the percentage error between the reconstructed and actual coordinates. Our methodology has undergone testing using various cell shapes, including ovals, ellipsoids, hemispheres, and complex base configurations.

2. System design and operational workflow

Figure 1 provides an illustrative overview of our complete imaging system. We employ a grating coupler—grooves in a waveguide—to couple free-space broadband light to the proposed slide and propagate in the desired direction to illuminate the cell. The grooves are strategically designed to efficiently couple transverse electric (TE)-polarized light from free-space visible light into the waveguide, including light from the built-in flashlight of a smartphone. Integrating the slide into a smartphone eliminates the need for an external light source, thus enhancing the system's portability. Furthermore, this grooved array structure serves as a wavelength filter, crucial for exciting fluorophores on the cell surface and avoiding background noise. Precise control over the wavelength is necessary to effectively excite the specific fluorophores used as labels and low-noise imaging techniques. Integrating this wavelength and polarization filtering capability into our designed slide obviates the need for external optical components. This approach not only simplifies the system but also significantly reduces costs. Notably, one of the significant expenses in micro-optical systems arises from aligning and assembling individual optical elements [27].

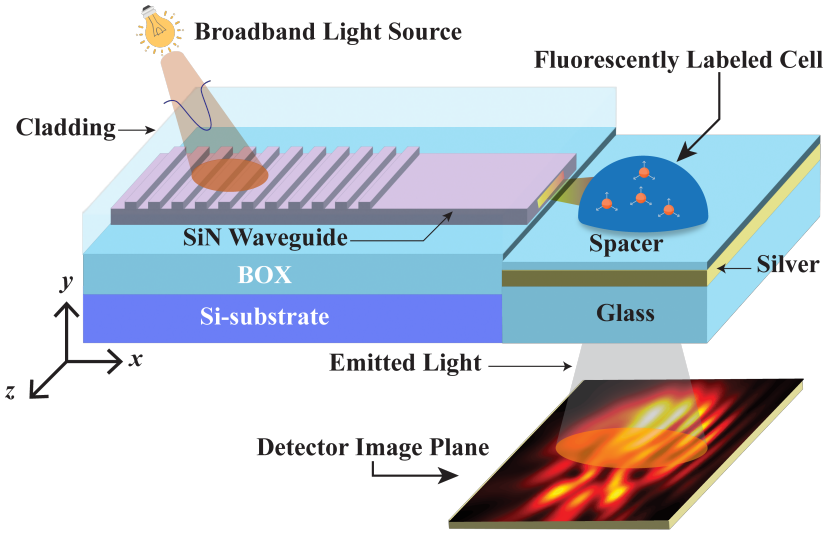

Fig. 1. Schematic illustration of the proposed imaging system.

Once the desired wavelength is filtered, the light is directed precisely to the location of the biological specimen—a cell. To achieve this, we design a SiN waveguide, primarily for its ability to efficiently couple light in the visible spectrum. SiN offers numerous advantages in the visible region, including low loss, minimal sensitivity to temperature fluctuations, compatibility with standard complementary metal oxide semiconductor (CMOS) technology, cost-effectiveness at large fabrication scales, and high integration density. This approach to illuminating the sample minimizes background noise in the acquired image, as direct light exposure from the source can introduce noise, leading to phototoxicity and photodamage during imaging [28].

The light coming from the waveguide couples to the cell and excites the fluorophores attached to the cell's surface. The cell is positioned on a planar SPCE setup consisting of a metal-dielectric layer. Fluorophores emit light upon excitation with a specific wavelength, resulting in the

Optics EXPRESS

generation of SPCE. The fluorescence light near 565 nm wavelength is detected on the structure's backside using either a charged-coupled device (CCD) camera or a CMOS detector. SPCE confines emitted light to specific angles relative to the surface. This directionality is advantageous for our imaging methodology, enabling efficient light collection and precise focusing with optical components like lenses. We employ a pair of convex lenses to focus this highly directional SPCE onto the detector's image plane. The lenses may be integrated into the slide to create a more compact and monolithic imaging system. By post-processing this circular spot on the detector, we determine the (x, y, z) coordinates of the fluorophores, corresponding to their positions on the cell's surface. This process enables the reconstruction of a 3D image of the cell. A detailed discussion of the imaging methodology will be provided in subsequent sections.

3. Slide design and simulation model

This section discusses the proposed imaging slide's design details and simulation models. Figure 2 presents a cross-sectional schematic illustration of the proposed slide structure. For convenience in discussion, we have divided the slide structure into the light-coupling structure and the cell placement or SPCE structure.

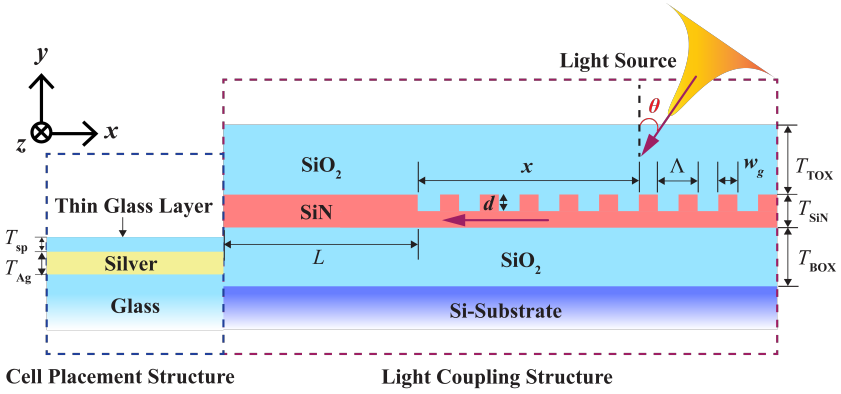

Fig. 2. Two-dimensional (2D) schematic view of the proposed structure.

The light coupling structure is a multilayered composition designed to efficiently couple light at 546 nm wavelength within the slide, matching the absorption peak of rhodamine B [29]. This structure consists of a 160 nm thick (T_{SiN}) SiN waveguide placed on a 700 nm thick (T_{BOX}) buried oxide (BOX) layer. The BOX layer, composed of silicon dioxide (SiO_2), rests upon a silicon (Si) substrate. Within the SiN waveguide layer, a grating has been created with groove depths (d) of 62 nm, a duty cycle of 40%, and a grating period (Λ) of 379 nm. The grating length is 15 μm, and the total number of gratings is 40. The grating is then covered with a 900 nm thick (T_{TOX}) cladding, index-matched to the BOX layer. Notably, the difference in refractive indices between SiN and SiO_2 gives rise to polarization selectivity in our grating coupler. We have optimized the grating coupler for TE polarization, i.e., the electric field vector of the coupled light is parallel to the grating, as it offers greater precision in determining the cell-surface coordinates [26]. Nevertheless, it is possible to design the grating coupler to couple the TM mode optimally if needed [30,31].

On the other side of the slide, we have an arrangement for cell placement, identical to the fundamental SPCE configuration detailed in Ref. [32]. As illustrated in Fig. 2, it comprises a planar layered structure designed to place the cell. The foundation of this structure begins with a bulk glass prism, onto which a 50-nm-thick (T_{Ag}) silver layer is deposited. Silver is the optimal choice for our design as it exhibits robust plasmonic properties at visible wavelengths.

Optics EXPRESS

These properties include a high extinction coefficient and a narrower plasmon resonance peak, significantly enhancing fluorescence emission when fluorophores are close to the silver surface. We have placed a 10-nm-thin (T_{sp}) SiO_2 atop the silver layer as a spacer layer. This layer serves a dual purpose: it protects the silver layer and mitigates the quenching effect on nearby fluorophores.

The fabrication of the proposed device is compatible with the standard CMOS manufacturing process. The fabrication of the structure can be released onto a silicon wafer, which serves as the initial substrate. After depositing the bottom SiO_2 layer onto the silicon (Si) substrate, the next step involves the deposition of a layer of SiN to create the waveguide. This deposition process can be effectively achieved using low-pressure chemical vapor deposition (LPCVD) [33,34]. The grating structure within the SiN layer can be defined through deep ultraviolet (DUV) optical lithography [35] and reactive ion etching (RIE) [36]. The cladding layer can be deposited atop the grating layer through plasma-enhanced chemical vapor deposition (PECVD) [37,38]. It is essential to etch both the top and bottom cladding layers and the waveguide to accommodate the cell placement structure on the Si substrate, which can be accomplished via the same groove-etching process. The Si substrate will serve as a stop layer during this process. A layer of glass-silver-glass must be deposited onto the Si substrate to form the cell placement structure. During deposition, precise alignment of the bottom glass layer with the Si substrate of the light coupling structure is required for mechanical stability. Finally, the Si substrate under the glass layer in the cell placement structure must be removed to allow imaging, as Si is opaque in the visible wavelength range. This removal can be done by patterning the Si substrate using backside alignment photolithography and then removing it using deep RIE [39]. Throughout this process, careful alignment of every layer ensures precision, resulting in the successful fabrication of the proposed device.

3.1. Simulation setup and parameter optimization

To comprehensively assess the performance of our designed slide and understand the coupled light's behavior, we employed the finite difference time domain (FDTD) method using Lumerical FDTD commercial software [40]. A 2D representation of our simulation setup is illustrated in Fig. 3. The refractive indices of the Si substrate, SiN, and SiO_2 were considered 4.12, 2.03, and 1.45, respectively. Our simulation setup for cell placement and cellular structures followed the configuration detailed in Ref. [41]. We modeled the cell as a hemispherical shape with a diameter of 1600 nm and a height of 400 nm. The cell surface has a 15-nm-thick membrane. Due to the computational limitations and high costs associated with simulating large volumes in Lumerical FDTD, we opted to model cells at a reduced scale. Nonetheless, our algorithm was applied to different cell sizes, and the results remained consistent, ensuring the validity of these smaller-scale simulations. The refractive index of the entire cell structure, including the intracellular components, was set to 1.38 [42]. This approximation simplifies the model, as the intracellular components do not significantly impact the results due to their small dimensions relative to the wavelength of the coupled light.

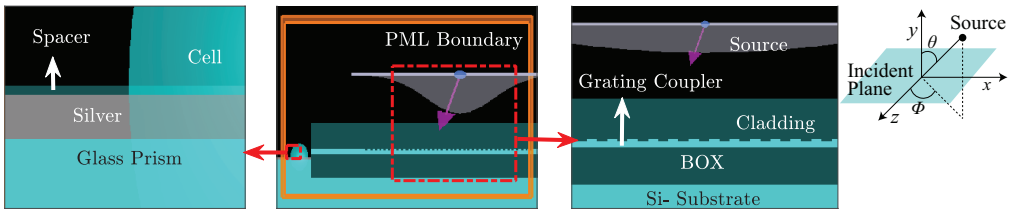

Fig. 3. A 2D schematic illustration of our designed structure's simulation setup.

Optics EXPRESS

Initially, we employed a 2D FDTD approach for waveguide design and grating coupler parameter optimization for less time and memory consumption. Notably, the cell placement structure was excluded from the optimization part, as it does not impact light coupling to the waveguide. The 2D simulation domain was set to 315 μm × 5 μm. Perfectly matched layers (PML) were employed as boundary conditions in all directions to absorb fields beyond the calculation area and minimize parasitic reflections. For this large simulation volume that supports strong resonances and takes a long time to decay, the maximum simulation time was set to 2500 fs. We used the default staircase mesh setting to define the simulation grid with a mesh accuracy of 3. Within the waveguide region, we overrode the FDTD mesh settings, employing a grid size of 0.01 μm in both the x and y directions to precisely capture closely spaced data points. Frequency domain power monitors were utilized in different directions to measure the in-coupling.

In our simulations, we modeled the amplitude distribution of the broadband incident light using a Gaussian source, covering a wavelength range from 350 to 750 nm. The Gaussian source was defined using thin lens calculations, with the numerical aperture (NA) set to 0.0265 and the focal point located at a distance of −3.2 μm. Proper setup of the source parameters is crucial for achieving optimal coupling efficiency. We systematically varied the incident beam angle (θ), representing the propagation angle relative to the source's incident axis, through a series of numerical computations. Figure 4(a) illustrates the variation of coupled power with θ at a wavelength of 546 nm. The highest coupling efficiency is observed at an incident angle of 15.5°. Following this, with the incident angle set to this optimal value, we varied the source polarization angle (ϕ), representing the orientation of the incident electric field, to maximize coupling efficiency, as depicted in Fig. 4(b). A polarization angle of zero degrees corresponds to p-polarized radiation, while a polarization angle of 90 degrees indicates s-polarized radiation. We varied the source's polarization angle from 0 to 90 degrees. The peak coupling efficiency was achieved at a polarization angle of 90 degrees, with a weighted average coupling efficiency of 27%. This analysis highlights that incident randomly polarized light achieves an approximate 27% coupling efficiency at 546 nm. To achieve maximum efficiency and selective fluorophore excitation, employing light with a polarization angle of 90 degrees is imperative.

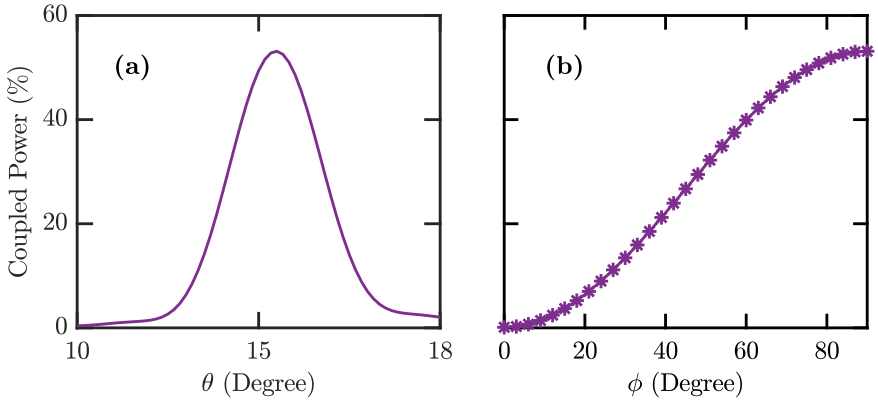

Fig. 4. Variation in power coupled to the waveguide with respect to (a) incident angle (θ) and (b) source polarization angle (ϕ) when λ = 546 nm.

Consequently, in the subsequent section, we will utilize the s-polarized incident beam tilted from the normal. Although vertical coupling offers advantages for system integration [43], aiming for perfect vertical coupling can lead to undesired reflections due to second-order Bragg diffraction [44]. Mitigating these reflections typically involves more complex fabrication processes due to the need for smaller feature sizes [45]. Therefore, positioning the source at an off-normal

Optics EXPRESS

angle relative to the surface improves efficiency and reduces back reflection. To optimize other structural parameters, we employed a particle swarm algorithm.

4. Result analysis

4.1. Characterization of the slide

Upon optimizing all design parameters, we investigated the performance of our slide with various light sources: a standard Gaussian beam, a white LED [46], and flashlights from Android (Samsung Galaxy A70) and iPhone (iPhone 11 Pro) [47]. Figure S1(a) in the Supplement 1 shows the spectral profiles of these sources, which were used to compute the coupling efficiency of the slide [48]. A power transmission monitor was placed at the end of the waveguide to measure the coupled power directly. We achieved a coupling efficiency of ~53% at the target wavelength of 546 nm, making the slide well-suited for imaging. As shown in Fig. S1(b), there is negligible variation in coupling efficiency and linewidth across the different source spectra. This observation confirms that the choice of source spectrum does not significantly affect results. Hence, in practical applications, any source spectra can be employed reliably. To simplify our simulations, we employed a Gaussian beam to model the overall structure and develop the imaging algorithm.

To gain deeper insight into the propagation characteristics, we measured the coupling efficiency for various lengths (l_w) within the waveguide, as depicted in Fig. 5(a). Additionally, an analysis of the intensity profile over a distance of 300 μm was performed, as shown in Fig. 5(b). The inset plot in Fig. 5(b) offers a detailed spatial distribution of the intensity profile along the y axis. Notably, the intensity and coupled power remain nearly constant within the waveguide region, validating the effective propagation of coupled narrowband light over several millimeters. To facilitate subsequent simulations during imaging, we set the waveguide length (L) to approximately 5 μm for further analysis. Notably, the imaginary part of the SiN refractive index remains negligible in the visible wavelength range, indicating minimal absorption. Therefore, any energy loss in the coupling process primarily arises from radiation loss. Various strategies can be explored to enhance further coupling efficiency, such as improving the diffraction directionality of the grating, which may involve integrating waveguide bottom mirrors [49], optimizing thickness and etching depth, or utilizing a metal reflector [50]. However, our primary priority is identifying the desired wavelength using a simplified structure rather than solely focusing on achieving the highest possible coupling efficiency. Therefore, we opted for a less-layered structure to facilitate a cost-effective and straightforward fabrication process.

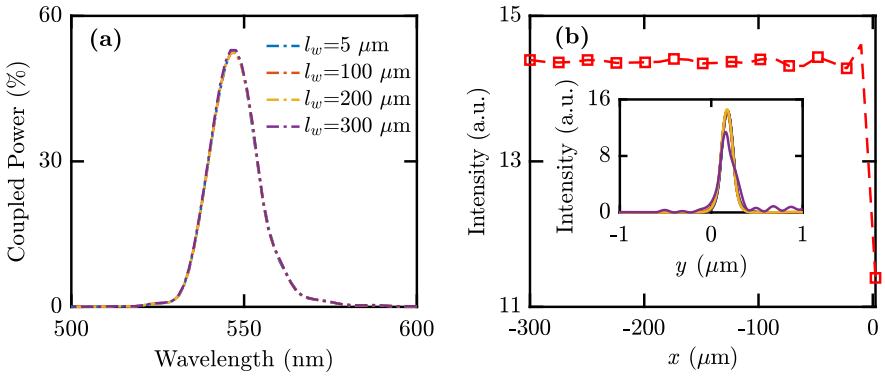

Fig. 5. (a) Coupled power as a function of wavelength at various lengths within the waveguide and (b) intensity profile along the x axis. The inset plot shows negligible intensity variation at different x positions across the y axis.

Optics EXPRESS

Figures 6(a) and (b) show the 2D field profiles of the structure in the xy and xz planes at $z = 0$ and $y = 0.2$ μm, respectively, illustrating that the light is mostly confined within the SiN waveguide region at our desired wavelength. Figure 6(c) shows that the electric field vector is directed in the z-direction, perpendicular to the plane of incidence, indicating that the light coupled to the waveguide is s-polarized. We also analyzed the field distribution in various structure regions to understand each field component's contribution. We observe that only the E_z component of the electric field, along with the H_x and H_y components of the magnetic field, are consistently present in all regions.

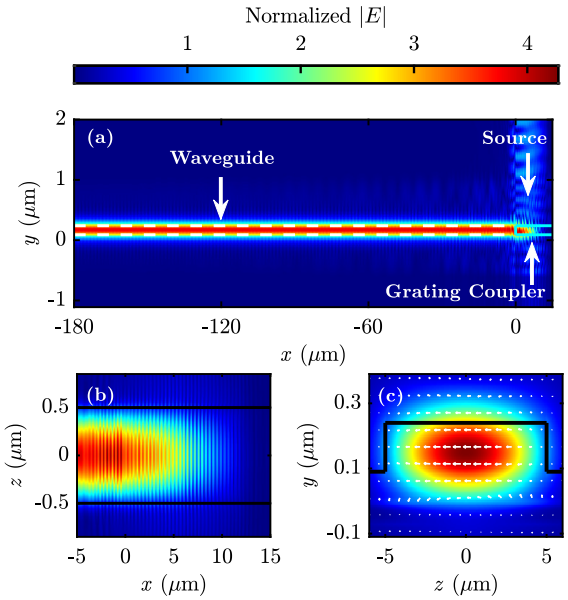

Fig. 6. Electric field distribution of the light coupling structure at $\lambda = 546$ nm in the (a) xy plane at $z = 0$ μm, (b) xz plane at $y = 0.2$ μm, and (c) yz plane at $x = -5$ μm. The axes orientation corresponds to that shown in Fig. 3.

4.2. *Characterization of the light coupled to the cell*

When a cell is placed on the slide with its base center at the (0,0,0) position, guided light from the waveguide impinges upon its surface and couples to the cell cavity. This section delves into the coupling of light to the cell. Following the design of the optimized slide, we conducted 3D simulations of the overall slide structure, including the cell. In 3D simulations, the total simulation volume was set to 20 μm × 5 μm × 2 μm. We investigated the coupled light at different cell sections and noted that ~17% of the incident light is coupled to the cell. Figure 7(a) presents the electric field profile at a wavelength of 546 nm in the xy plane at $z = 0$ in the presence of the cell, demonstrating how light couples to the cell from the waveguide.

A detailed analysis of the intensity and electric field distribution across the cell surface is crucial to understanding how light behaves when a fluorophore is positioned on the cell's membrane. We accomplish this by examining the coupled light in four xz planes at $y = 90, 190, 290$, and 390 nm, set above the cell's base. Figures 7(b)–(e) illustrate the electric field distribution across different cross-sections within the cell, with dashed lines indicating the cell boundary. In Fig. 7(b), at a height near the cell's base ($y = 90$ nm), the intensity is the highest on the right and left sides, primarily due to the metal layer exposed near the cell and influenced by the cell's edges. The maximum intensity is observed at a height of 190 nm, aligned with the waveguide center position,

Optics EXPRESS

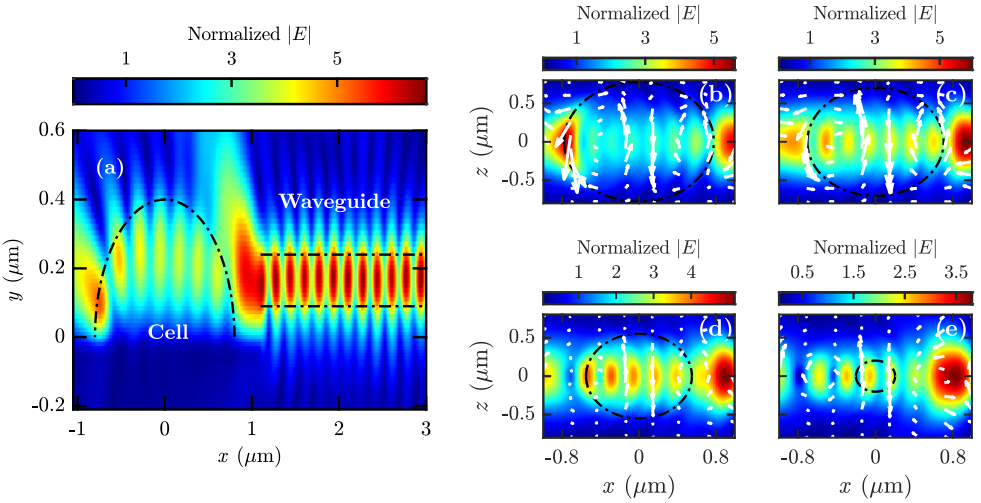

Fig. 7. (a) Near-field profile in the xy-plane when the cell is placed on the slide at $\lambda = 546$ nm and (b)–(e) near-field profiles for different cross sections in the xz plane for (b) $y = 90$ nm, (c) $y = 190$ nm, (d) $y = 290$ nm, and (e) $y = 390$ nm. The axes orientation corresponds to that shown in Fig. 3.

as shown in Fig. 7(c). In Figs. 7(d) and (e), the intensity gradually decreases toward the top of the cell, mainly because the waveguide height is smaller than the cell's height. The intensity consistently decreases in the z-direction away from $z = 0$ as the cell's diameter exceeds the waveguide's width, which does not significantly affect imaging.

By dividing the entire cell into two regions based on the azimuthal angle, with θ ranging from 0 to π and from π to 2π, it becomes apparent that intensity is symmetrically distributed in these regions. Thus, the impact on fluorophore excitation is equivalent in both regions. Consequently, we can consider only half of the cell when determining the cell surface coordinates. Additionally, the coupled light is polarized in the z-direction, as observed in Figs. 7(b)–(e), aligning with the gratings of the waveguide. This implies that the fluorophore on the cell surface will be excited by s-polarized light.

4.3. *Excitation-dependent emission behavior of rhodamine B*

In practice, cells are labeled with fluorophores by immersing them in a solution containing specific fluorophores. In simulations, we have placed rhodamine B, i.e., electric dipoles, over the cell surface. However, before discussing the imaging process, it is crucial to discuss how the coupled light to the cell excites fluorophores and affects their emission patterns. This is particularly important because the intensity over the cell surface is not uniformly distributed.

We employ a semi-classical approach, utilizing Lumerical FDTD, to model the interaction between the incident field and fluorophores. A schematic representation of the simulated structure is provided in Fig. S2 of the Supplement 1. In this framework, fluorescent molecules are treated as a four-level quantum system. Transitions between these levels are governed by coupled rate equations, while Maxwell's equations describe the behavior of electromagnetic waves (see Supplement 1). Although real fluorophores may involve many energy levels, a four-level atomic system emulates the fluorophore behavior sufficiently [51]. The kinetic parameters are tailored to this four-level model to match the maximum emission wavelength. Specifically, the parameters for the four-level atomic system are chosen as follows: Transition wavelengths $\lambda_{30} = 546$ nm and $\lambda_{21} = 565$ nm; transition lifetimes $\tau_{30} = 5$ ns, $\tau_{21} = 3$ ns, $\tau_{32} = 0.3$ ps, and $\tau_{10} = 0.35$ ps; and

Optics EXPRESS

dephasing times $T_{30} = 9$ fs and $T_{21} = 25.5$ fs. The population density is initially at the ground state with a density of 5.022×10^{23} m^{-3}.

We utilize a pump-probe approach to determine the emission characteristics of rhodamine B dyes. The pumping beam, with a frequency corresponding to λ_{30}, excites molecules from the ground state level (N_0) to the third quantum mechanical energy level (N_3). Subsequently, a rapid non-radiative transition occurs between the highest level (N_3) and the level below it (N_2). Following a certain time delay, we probe the medium with a center frequency equal to the emission wavelength of rhodamine B (λ_{21}) to estimate system amplification. The probe pulse is significantly weaker than the pump pulse and drives molecules from N_2 to N_1. Finally, molecules undergo rapid non-radiative transfer from N_1 to N_0.

The maximum transmission occurs at the emission wavelength of rhodamine B, specifically at 565 nm [52], as shown in Fig. 8(a). To investigate the impact of the excitation field intensity on emission, we systematically vary the excitation field's intensity and measure the resulting emission intensity using a power monitor. Figure 8(b) shows the relationship between the excitation and emission intensities for the modeled fluorophore, revealing a linear correlation up to a certain threshold beyond which emission becomes saturated. This relationship forms the basis for setting the electric dipole's emission intensity, ensuring our imaging system's validity. Additionally, coupling s-polarized light to the cell results in preferential excitation of molecules whose transition moment parallels the incoming polarized light. Consequently, the emission of excited molecules' dipoles is preferentially oriented concerning the electric vector of the stimulating radiation. Therefore, our imaging algorithm development incorporates a monolithic simulation employing a horizontally oriented dipole moment with the measured intensity.

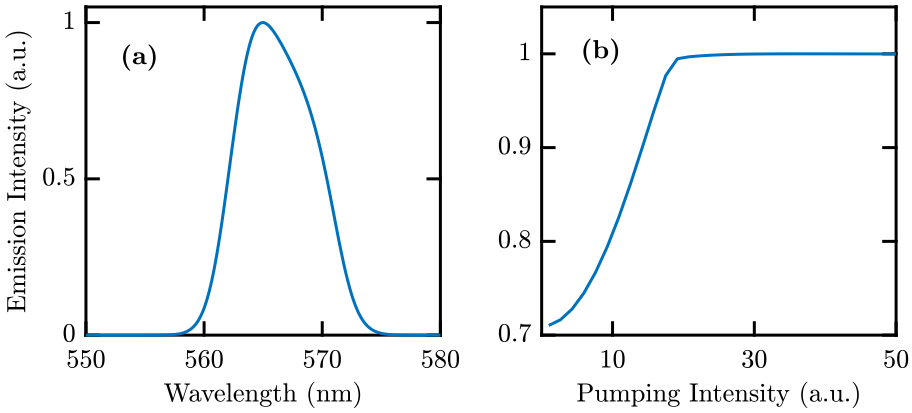

Fig. 8. (a) Normalized emission from the modeled fluorophore as a function of the wavelength and (b) relationship between the excitation and emission intensities.

When the incident light is s-polarized and the fluorophores are randomly oriented, the interaction between the incident light and the fluorophores will lead to selective excitation of only those fluorophores whose transition dipole moments are aligned parallel to the polarization direction of the incident light. Fluorophores with transition dipole moments oriented perpendicular to the polarization direction of the incident light will not be effectively excited.

5. Imaging methodology

Our proposed imaging technique aims to reconstruct the cell's surface by determining the (x, y, z) coordinates of fluorophores attached to the cell membrane. While our approach draws inspiration from the methodology outlined in Ref. [26], we have made significant advancements to enhance its applicability to real-world scenarios. Unlike previous assumptions of uniform emission

Optics EXPRESS

intensity for fluorophores, our algorithm incorporates excitation-dependent emission profiles to ensure effectiveness in practical conditions. By considering the relative emission intensity of fluorophores, we enhance the robustness of our algorithm. Furthermore, unlike Ref. [26], which employs both s- and p-polarized light for excitation, we focus solely on s-polarized excitation for determining the fluorophore's y coordinate. This simplification minimizes the complexity associated with sequential excitation, facilitating more efficient data acquisition and streamlining the process. Furthermore, we have expanded our analysis from single-cell imaging to the 3D imaging of clustered cells, demonstrating the applicability of our method in more complex scenarios.

Another key enhancement is the incorporation of narrowband filtering within the slide, which effectively reduces noise by preventing direct broadband light exposure. Broadband excitation can cause light to couple to surface plasmons at various angles, resulting in emitted light focusing at multiple points along the optical axis, leading to blurred and spread-out spots on the image plane and reducing imaging accuracy. In contrast, narrowband excitation ensures that SPCE is tightly focused into a single point, significantly improving the precision of coordinate determination. Figure 9 shows how narrowband filtering by the designed slide reduces noise and enhances the sharpness of the SPCE spot compared to broadband excitation of fluorophores.

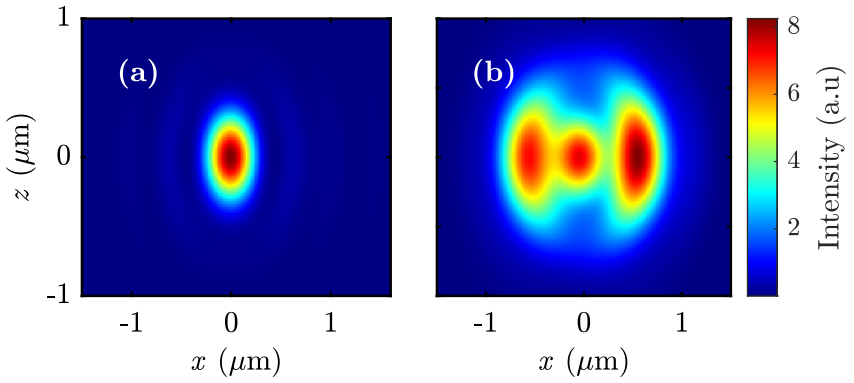

Fig. 9. Reconstructed spots on the image plane with (a) light exposure using the designed slide, resulting in a sharply focused spot, and (b) direct light exposure, leading to a diffused spot.

The imaging methodology begins with detecting the highly directional SPCE emission and converging it into a circular spot using two convex lenses. The first lens collects the emitted light and decomposes it into parallel plane waves propagating at different angles. The second lens converges these plane waves into a circular spot on the image plane. To simulate the behavior of the first lens, we numerically calculate the near-field data and decompose it into plane waves. A field monitor, positioned 300 nm below the cell, is used to collect the near-field data. We assume a numerical aperture (NA) of 0.7 and discard any plane waves with angles outside this range. The remaining plane waves are then recombined using the inverse chirped z-transformation (ICZT) to create an image on the image plane, similar to the second lens's behavior. Subsequent post-processing of the converged image plane data facilitates determining (x, y, z) coordinates. Figure 10 provides an overview of the workflow for determining the coordinates.

5.1. Determining fluorophore's (x, z) coordinates for imaging cell base

To determine the fluorophore's (x, z) coordinates, we applied an approach similar to that described in Ref. [26], but the fluorophore emission intensity varies based on the light pattern coupled in the cell. We used this approach to determine the fluorophore's (x, z) coordinates based on the

Optics EXPRESS

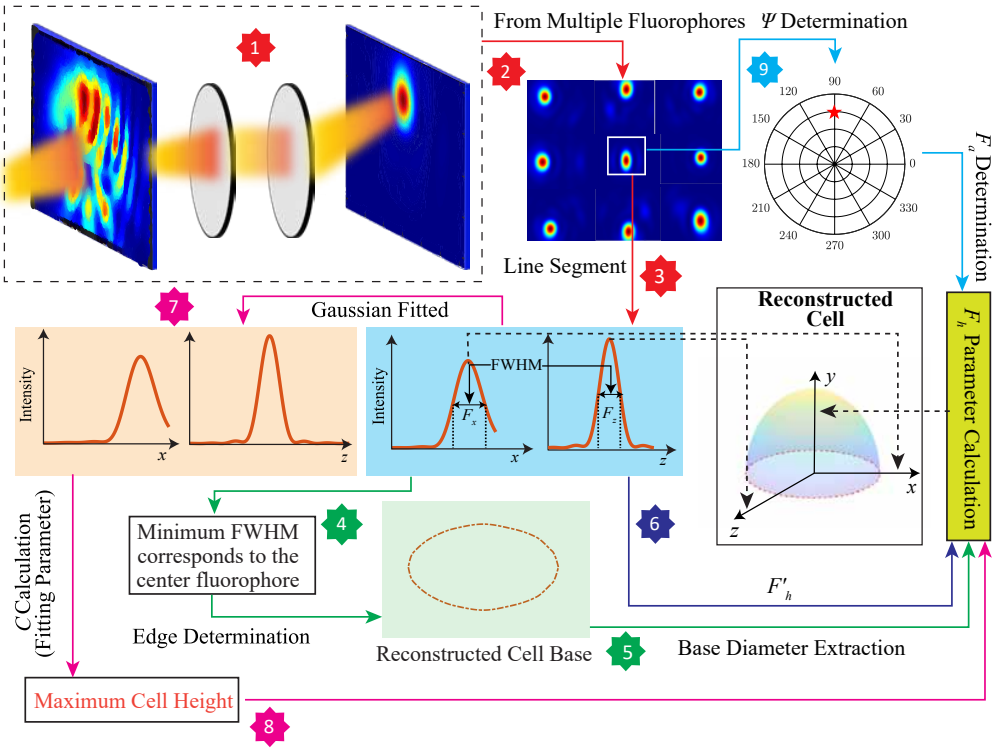

Fig. 10. Schematic diagram of the 3D cell imaging process, illustrating the detection of the x, z coordinates of fluorophores (steps 1–3), followed by edge determination and cell base diameter calculation (steps 4–5). Gaussian fitting is then applied to determine the maximum cell height and other parameters, leading to the final determination of the y coordinate and subsequent 3D cell reconstruction (steps 6–9).

maximum intensity location within the converged circular spot on the xz plane, as shown in step 1 in Fig. 10. We also can reconstruct the cell base through the (x, z) coordinate determination process. The cell base refers to the portion of the cell's surface in contact with the spacer layer. The reconstruction of the cell base allows us to calculate the diameter of the base, providing insights into the overall cell size. Additionally, knowing the cell's diameter is a prerequisite to ascertaining its height. As the cell is labeled with multiple fluorophore markers, the image plane will exhibit several circular spots upon converging onto the image plane. Each spot corresponds to a specific point on the cell surface. Therefore, accurately identifying the base points among these points is crucial for precise reconstruction. To do this, we initially identified the fluorophore at the topmost position as the reference point for our analysis. After detecting the peak fluorophore, we determined the fluorophore positions at the edge of the cell surface, following the same process discussed in Ref. [26].

We simulated two ellipsoidal cell shapes with a base diameter of $w = 1600$ nm for each cell and heights of $h = 400$ nm and 600 nm. The intensity distribution of the peak fluorophore compared to the other fluorophores along the x and z axes is shown in Figs. 11(a) and (b), respectively. From these curves, we calculated the full width at half maximum (FWHM) and plotted it in Figs. 11(c) and (d). Regardless of the cell's size, it is evident from these figures that the fluorophore at the center, i.e., $\phi = 0$ and $\phi = 90°$ in the x and z directions, respectively, has the smallest FWHM, helping the detection of the peak fluorophore. Therefore, by determining the topmost dye, we

Optics EXPRESS

can locate the base point (x, z) and reconstruct the cell base. The cell's diameter can be measured by calculating the difference between the minimum and maximum coordinate values.

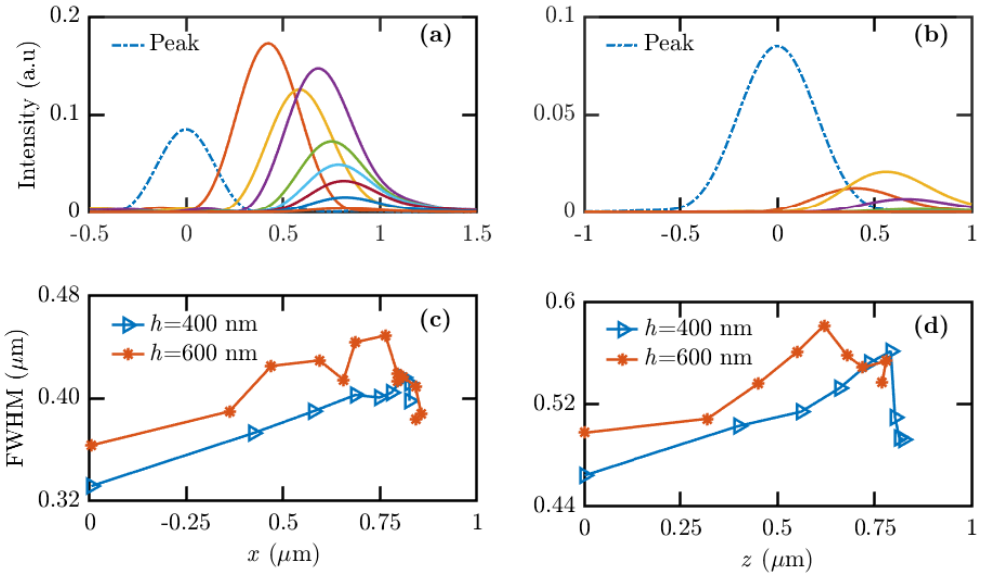

Fig. 11. Intensity distribution of the converged spot for locating the fluorophore at different positions along (a) x axis and (b) z axis. FWHM of the converged spot against the fluorophore position in the (c) x direction ($\phi = 0$) and (d) z direction ($\phi = 90°$). FWHM is obtained for cell heights of 400 nm and 600 nm, while the diameter remains constant at 1600 nm in both directions.

To validate our approach, we conducted simulations for different cell structures, including hemispherical, ellipsoidal, and irregular shapes. Table S1 presents a subset of base points (x, z) for a hemispherical cell. Although only a few points are displayed for brevity, numerous additional fluorophore positions were detected to recreate the entire base shape. Figure 12(a) shows the recreated base shape. The root mean square error (RMSE) for the x and z coordinates is found to be $< 1.15\%$ and $< 1.71\%$, respectively. Figure 12(b) shows the base images of an ellipsoidal cell shape, with a diameter of 1000 nm along the x direction (w_x), 500 nm along the z direction (w_z), and $h = 400$ nm. The calculated RMSE for the ellipsoidal cell is $< 0.736\%$ for the x coordinate and $< 0.795\%$ for the z coordinate. Additionally, we have determined base images for irregular-shaped cells, as shown in Fig. 12(c). The maximum RMSE for the recreated irregular cell bases is $< 3\%$ for the x and z coordinates. These images of irregular-shaped cells demonstrate the feasibility of our proposed technique for realistic scenarios where cells, especially unhealthy ones, may have irregular shapes and sizes. Thus, this approach allows for the reconstruction of cell bases with minimal error.

5.2. *Determining fluorophore's y coordinate*

The fluorophores' intensity distributions on the image plane can be effectively described by Gaussian curves in the x and z directions. By analyzing the Gaussian fit to the intensity distribution, we developed equations to determine the y coordinate of the fluorophore. This analysis enabled us to accurately determine the cell's height (H) and the vertical position of each fluorophore, contributing to the overall reconstruction of the cell's shape and structure.

Optics EXPRESS

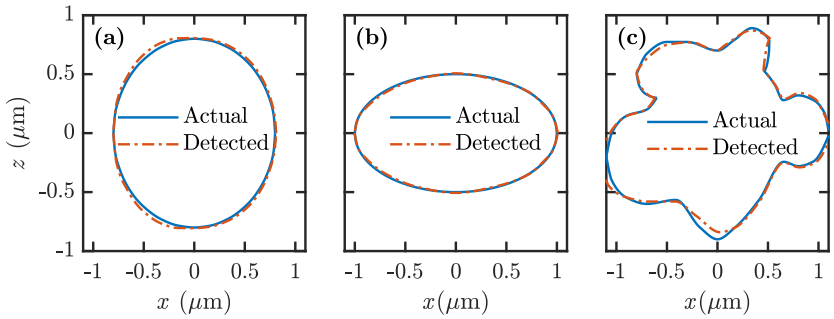

Fig. 12. Comparison between actual and detected bases of various cell bases with (a) circular, (b) elliptical, and (c) irregular shapes.

5.3. Determination of cell height

In the previous section, we discussed determining the (x, z) coordinates of the fluorophore located at the cell's peak, which corresponds to the topmost position of the cell. Once we have detected the fluorophore at the topmost position, its y coordinate indicates the cell's height. Figure 13(a) presents the reconstructed spot on the image plane after convergence. From Fig. 13(b) and (c), we observe that the intensity distribution of the fluorophores on the image plane follows a Gaussian curve in the x and z directions. Therefore, we performed curve fitting to the intensity distribution data by employing the Gaussian equation given by

$$f(x) = a \exp\left[\frac{-(x-b)^2}{c^2}\right], \tag{1}$$

where a represents the amplitude of the Gaussian distribution, b represents the mean of the distribution, and c represents the standard deviation of the distribution. Figures 13(b) and (c) illustrate that the Gaussian curves fit the intensity distribution data well. Extracting the c parameter from the curve fitting equation, we can determine the maximum height of the cell using the following equation

$$C = \sqrt{|c_x - c_z| \times c_z}, \tag{2}$$

where c_x and c_z are the c parameters from the intensity distribution that fits in the x and z directions, respectively.

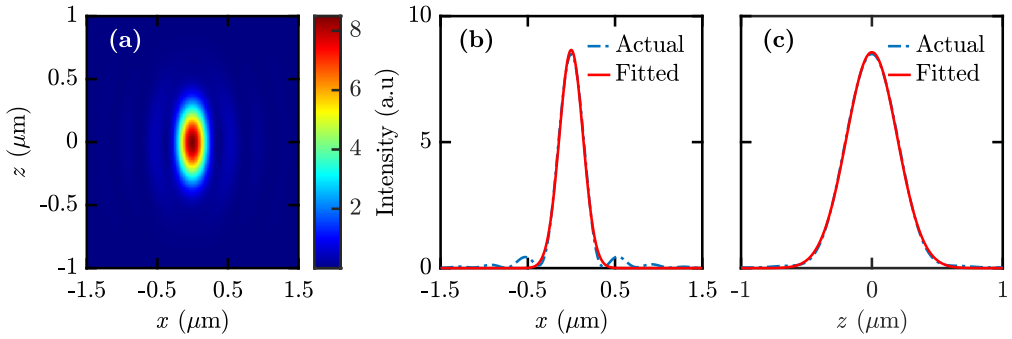

Fig. 13. (a) Reconstructed spot of the peak fluorophore on the image plane. Actual and Gaussian fitted intensity $|Ex|^2+|Ey|^2+|Ez|^2$ distribution along (b) x axis and (c) z axis.

Equation (2) was derived based on extensive observations and analyses across various parameter regimes, revealing a consistent pattern in the C parameter. We found that when the cell's height

Optics EXPRESS

(H) and base radius (r) are kept constant, C remains nearly the same, indicating a stable relationship with the ratio of the cell's height to its radius, denoted as R_c. However, C varies with individual changes in the cell's height and base radius. To investigate this further, we calculated C for different base diameters while keeping the height constant. Subsequently, we determined the average value of C for specific R_c values associated with different heights and base radii. Figure S3 illustrates the variation of C with respect to R_c. Referring to the data presented in Fig. S3, we can determine the R_c value corresponding to a calculated C.

We can precisely calculate the cell's maximum height by multiplying the R_c value by the cell's base radius. This calculation holds for cells with a circular base, where the base radius in the x-direction (r_x) is equal to the radius in the z-direction (r_z). However, for cells with unequal r_x and r_z, R_c needs to be multiplied by the ratio of cell radius in the x and z directions. We employed the approach described in the previous section to determine the cell's base radius (r). Table S2 (Supplement 1) presents various examples of C and corresponding R_c values obtained from the analysis. The cell height is calculated using the R_c value and the base radius of each cell. The error column indicates the percentage difference between the estimated and actual cell heights.

5.4. Vertical position (y coordinate) of each fluorophore

We have already calculated the (x, z) coordinates of the fluorophore. Determining the y coordinate is essential for 3D imaging of the cell. The intensity distribution of the converged spot on the image plane is similar to the Gaussian curve and exhibits a line width. Using the full width at half maximum (FWHM) and the b parameter from the Gaussian fitting of the circular spot of a fluorophore on the image plane, we can determine the y coordinate of other fluorophores. The following points outline the procedure for determining the y coordinate of the fluorophore.

1. **Calculation of F'_h**: Each spot on the xz plane is analyzed by calculating F'_h, which is determined as
$$F'_h = |F_x + F_z + x + z|. \tag{3}$$
Here, F_x represents the FWHM of the spot along the x axis, F_z represents the FWHM along the z axis, and x and z are the respective coordinates of the spot and can be determined as described in Sec. 5.1.

2. **Determination of the polar angle ψ:** Fluorophores located in any position except the center of the image plane converge at an angle, denoted as ψ. The polar angle (ψ) is determined by converting the Cartesian coordinates (x, z) of the spot to polar coordinates.

3. **Identification of the coefficient value F_a:** F_a corresponds to the value of $F_{h'}$ at the base point. Our observations showed that the coefficient value F_a remains constant for a specific ψ, regardless of the cell size. To determine the exact value of F_a for a given spot, we refer to the ψ vs. F_a plot given in Fig. S4(a) (Supplement 1). This plot provides insights into the relationship between the coefficient value F_a and different polar angles, which greatly assists in accurately determining the y coordinate of the fluorophore.

4. **Calculation of F_h:** Using the obtained F_a, we calculate $F_h = F'_h/F_a$. Notably, F_h remains constant when the relative vertical position of the fluorophore, h' (calculated as y/H, where y is the vertical position of the fluorophore and H is the maximum cell height), remains fixed, regardless of the cell size or fluorophore's position on the xz plane. However, as h' varies, F_h values undergo distinct changes. Multiple arbitrary cell samples were simulated to comprehensively investigate this behavior, with fluorophores placed at random positions. F_h was calculated and averaged for specific h' values for each case. The resulting averaged F_h values were then plotted against the corresponding h' values, giving us the F_h vs. h'

Optics EXPRESS

curve shown in Fig. S4(b) Supplement 1). This curve is a useful reference for determining each fluorophore's h' value based on its F_h value.

Table S3 presents the relative vertical position (h') of fluorophores at various random locations on the cell surface for different cell sizes, determined using the procedure discussed above. If the cell height is constant, h' varies little with the y-position. However, it varies when the y-position changes. However, as indicated in Table S3, h' varies when the y-position of the fluorophores changes. Accurately determining h' is essential for precisely determining the y coordinate of the fluorophores, significantly contributing to achieving high-fidelity 3D imaging of the cell.

5. **Determination of the y coordinate:** The obtained h' value is multiplied by H, resulting in the y coordinate of the fluorophore.

By following these steps, the y coordinate of each fluorophore can be accurately determined, facilitating comprehensive 3D imaging of the cell. This approach leverages the analysis of intensity distribution, Gaussian fitting parameters, and spatial characteristics of the fluorophores, allowing for precise reconstruction of the cell's 3D structure in research applications.

5.5. 3D imaging of individual and clustered cells using the proposed methodology

We applied our methodology to achieve accurate 3D reconstruction of both individual and clustered cells. For individual cell imaging, we modeled an ellipsoidal cell with dimensions of 1600 nm in the x and z directions and 400 nm in the y direction, labeled with fluorophores, as shown in Fig. 14(a). For discussion, we focus on a specific fluorophore located at $(0.37, 0.25, 0.51)$ μm. Following the method described in Sec. 5.1, we determined the (x, z) coordinates of the fluorophore and reconstructed the cell's edge coordinates and base shape. To determine the y coordinate, we converted the spot's Cartesian coordinates (x, z) to polar coordinates, revealing that the spot was positioned at a polar angle of 53.95°. Referring to Fig. S4(a) (Supplement 1), we identified the corresponding coefficient value F_a as 2.03 μm. Next, we calculated F'_h as 1.81 μm and obtained $F_h = 0.894$ by dividing F'_h by F_a. This F_h value corresponds to $h' = 0.633$, as shown in Fig. S4(b). Using the procedure described in Sec. 5.3, we determined the cell height H to be 0.408 μm and multiplied it by h', resulting in a y coordinate of 0.258 μm for the fluorophore. The reconstructed coordinates for the fluorophore are $(0.392, 0.258, 0.517)$, with percentage errors of (0.443, 3.306, 2.046) compared to the actual values. For clarity, a complete workflow and corresponding simulation results are provided in Fig. S5. Applying this procedure to multiple fluorophores on the cell surface, we reconstructed the cell's 3D structure, as presented in Fig. 14(b). Table 1 compares the actual and reconstructed 3D coordinates, including percentage errors, demonstrating the accuracy of our approach.

Table 1. Comparison of actual and reconstructed cell coordinates using the proposed methodology with percentage error

Actual (x, y, z) (μm)	Calculated (x, y, z) (μm)	Error (x, y, z) (%)
(0.6930, 0.2, 0)	(0.7336, 0.2093, 0)	(5.8529, 4.6520, 0)
(0.2324,0.35, 0.2911)	(0.2527, 0.3607, 0.31)	(8.7623,3.0491, 6.4882)
(0.3651, 0.25, 0.5066)	(0.3923, 0.2583, 0.517)	(7.4410, 3.3056, 2.0465)
(0.5085, 0.05, 0.6094)	(0.5164, 0.0490, 0.62)	(5.2586, 8.88, 1.0634)
(−0.4378,0.15, 0.5986)	(−0.4608, 0.1367, 0.605)	(0.594, 1.264, 1.884)
(−0.5421, 0.05, 0.5797)	(−0.5538, 0.0490, 0.6)	(2.1581, 2.08, 3.4972)

Optics EXPRESS

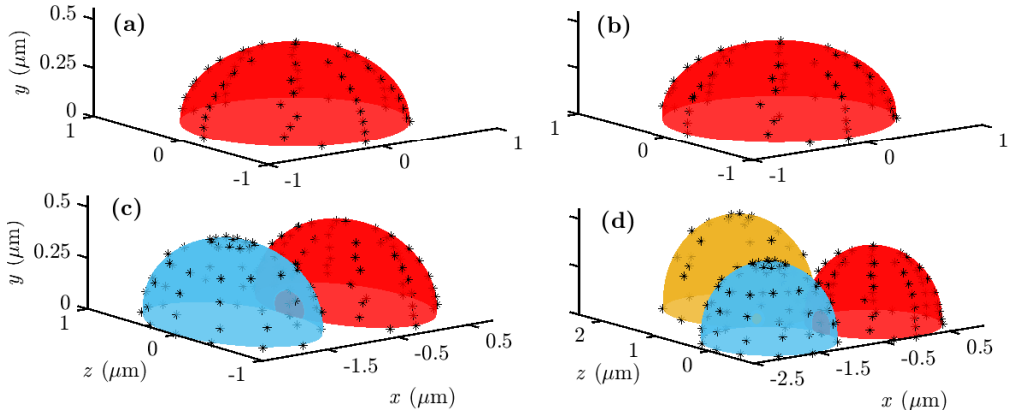

Fig. 14. 3D imaging of cells using the proposed methodology. (a) Actual and (b) reconstructed single cell; (c) reconstructed two-cell cluster, each cell with dimensions $w_x = w_z = 1600$ nm and $H = 400$ nm; (d) reconstructed three-cell cluster with two cells of the same dimensions as in (c) and one cell with dimensions $w_x = w_z = 1800$ nm and $H = 500$ nm.

We extended our algorithm to reconstruct 3D images of clustered cells. Each cell is labeled with multiple fluorophores, and their x and z coordinates are determined as before. We applied the DBSCAN clustering algorithm to group these coordinates and performed geometric fitting to detect circular or ellipsoidal patterns corresponding to the shapes of individual cells. After identifying the number of cells in the cluster, we used the same imaging process as with individual cells to reconstruct the 3D structure of the entire cell cluster. Figure 14 illustrates the reconstructed 3D images of individual and clustered ellipsoidal cells, demonstrating our methodology's ability to accurately reproduce cellular 3D structures and the spatial fluorophore distribution. This approach offers significant insights into cellular architecture and facilitates precise investigations in cell biology.

6. Conclusion

In conclusion, we have developed a compact, cost-effective, and portable fluorescent cell imaging system, designed to deliver precise three-dimensional biological cell imaging. By integrating a specialized slide with an advanced image processing algorithm, our system achieves high accuracy with minimal background noise and consistently low RMSE values across various cell shapes, including ovals, ellipsoids, hemispheres, and more complex configurations. While this work focuses on cell surface reconstruction, intra-cellular organelles can be imaged using membrane-permeable fluorophore labeling. By bridging the gap between cutting-edge research and practical applications, we believe our imaging system will play a crucial role in advancing cellular analysis and biomedical research, offering valuable insights into cellular morphology and disease diagnostics.

Acknowledgment. M. Momtaj acknowledges the M.Sc. fellowship she received during this research, supported by the Bangladesh University of Engineering and Technology (BUET) and the Forum-85 BUET Alumni.

Disclosures. The authors declare no conflicts of interest.

Data availability. Data underlying the results presented in this paper are not publicly available at this time but may be obtained from the authors upon reasonable request.

Supplemental document. See Supplement 1 for supporting content.

Optics EXPRESS

References

1. T. Imamura, T. Saitou, and R. Kawakami, "In vivo optical imaging of cancer cell function and tumor microenvironment," Cancer Sci. **109**(4), 912–918 (2018).
2. S. McTighe and I. Chernev, "Intramuscular lipoma: a review of the literature," Orthop. Rev. **6**(4), 5618 (2014).
3. K. M. Dalal, C. R. Antonescu, and S. Singer, "Diagnosis and management of lipomatous tumors," J. Surg. Oncol. **97**(4), 298–313 (2008).
4. M. Alhasan and M. Hasaneen, "Digital imaging, technologies and artificial intelligence applications during covid-19 pandemic," Comput. Med. Imaging Graph. **91**, 101933 (2021).
5. M. Kubánková, B. Hohberger, J. Hoffmanns, *et al.*, "Physical phenotype of blood cells is altered in covid-19," Biophys. J. **120**(14), 2838–2847 (2021).
6. V. Varadarajan, M. Shabani, B. Ambale Venkatesh, *et al.*, "Role of imaging in diagnosis and management of covid-19: a multiorgan multimodality imaging review," Front. Med. **8**, 765975 (2021).
7. A. Umar and S. Atabo, "A review of imaging techniques in scientific research/clinical diagnosis," MOJ Anat. Physiol. **6**(5), 175–183 (2019).
8. J. Wallyn, N. Anton, S. Akram, *et al.*, "Biomedical imaging: principles, technologies, clinical aspects, contrast agents, limitations and future trends in nanomedicines," Pharm. Res. **36**(6), 78 (2019).
9. T. Ahmed, S. J. R. Rizvi, S. Rasheed, *et al.*, "Digital health and inequalities in access to health services in bangladesh: mixed methods study," JMIR mHealth and uHealth **8**(7), e16473 (2020).
10. S. A. Boppart and R. Richards-Kortum, "Point-of-care and point-of-procedure optical imaging technologies for primary care and global health," Sci. Transl. Med. **6**(253), 253rv2 (2014).
11. J. Balsam, M. Ossandon, H. A. Bruck, *et al.*, "Low-cost technologies for medical diagnostics in low-resource settings," Expert Opin. Med. Diagn. **7**(3), 243–255 (2013).
12. S. Nayak, N. R. Blumenfeld, T. Laksanasopin, *et al.*, "Point-of-care diagnostics: recent developments in a connected age," Anal. Chem. **89**(1), 102–123 (2017).
13. H. Zhu, S. O. Isikman, O. Mudanyali, *et al.*, "Optical imaging techniques for point-of-care diagnostics," Lab Chip **13**(1), 51–67 (2013).
14. S. W. Paddock, "Confocal laser scanning microscopy," BioTechniques **27**(5), 992–1004 (1999).
15. M. A. Neil, R. Juškaitis, and T. Wilson, "Method of obtaining optical sectioning by using structured light in a conventional microscope," Opt. Lett. **22**(24), 1905–1907 (1997).
16. Y. Chen, W. Liu, Z. Zhang, *et al.*, "Multi-color live-cell super-resolution volume imaging with multi-angle interference microscopy," Nat. Commun. **9**(1), 4818 (2018).
17. E. H. Stelzer, F. Strobl, B.-J. Chang, *et al.*, "Light sheet fluorescence microscopy," Nat. Rev. Methods Primers **1**(1), 73 (2021).
18. N. Bourg, C. Mayet, G. Dupuis, *et al.*, "Direct optical nanoscopy with axially localized detection," Nat. Photonics **9**(9), 587–593 (2015).
19. H. Schneckenburger and V. Richter, "Challenges in 3D live cell imaging," in *Photonics*, vol. 8 (2021), p. 275.
20. S. Andersson-Engels, C. Klinteberg, K. Svanberg, *et al.*, "In vivo fluorescence imaging for tissue diagnostics," Phys. Med. Biol. **42**(5), 815–824 (1997).
21. S. Wang, W. X. Ren, J.-T. Hou, *et al.*, "Fluorescence imaging of pathophysiological microenvironments," Chem. Soc. Rev. **50**(16), 8887–8902 (2021).
22. W.-P. Cai, Q. Liu, S.-H. Cao, *et al.*, "Prism-based surface plasmon coupled emission imaging," ChemPhysChem **13**(17), 3848–3851 (2012).
23. S.-H. Cao, W.-P. Cai, Q. Liu, *et al.*, "Surface plasmon–coupled emission: what can directional fluorescence bring to the analytical sciences?" Annu. Rev. Anal. Chem. **5**(1), 317–336 (2012).
24. M. Chen, S.-H. Cao, and Y.-Q. Li, "Surface plasmon–coupled emission imaging for biological applications," Anal. Bioanal. Chem. **412**(24), 6085–6100 (2020).
25. Y.-Q. Li, S.-H. Cao, W.-P. Cai, *et al.*, "Directional fluorescence based on surface plasmon-coupling," Rev. Fluoresc. **8**, 71–95 (2016).
26. A. Mazumder, M. Mozammal, and M. A. Talukder, "Three-dimensional imaging of biological cells using surface plasmon coupled emission," J. Biomed. Opt. **27**(10), 106002 (2022).
27. J. Backlund, J. Bengtsson, C.-F. Carlström, *et al.*, "Input waveguide grating couplers designed for a desired wavelength and polarization response," Appl. Opt. **41**(15), 2818–2825 (2002).
28. J. Icha, M. Weber, J. C. Waters, *et al.*, "Phototoxicity in live fluorescence microscopy, and how to avoid it," BioEssays **39**(8), 1700003 (2017).
29. F. Vult von Steyern, J.-O. Josefsson, and S. Tågerud, "Rhodamine B, a fluorescent probe for acidic organelles in denervated skeletal muscle," J Histochem Cytochem. **44**(3), 267–274 (1996).
30. G. Dabos, A. Manolis, A. Giesecke, *et al.*, "TM grating coupler on low-loss LPCVD based Si_3N_4 waveguide platform," Opt. Commun. **405**, 35–38 (2017).
31. Z. Xiao, F. Luan, T.-Y. Liow, *et al.*, "Design for broadband high-efficiency grating couplers," Opt. Lett. **37**(4), 530–532 (2012).
32. N. Calander, "Theory and simulation of surface plasmon-coupled directional emission from fluorophores at planar structures," Anal. Chem. **76**(8), 2168–2173 (2004).

Optics EXPRESS

33. C. R. Doerr, L. Chen, Y.-K. Chen, *et al.*, "Wide bandwidth silicon nitride grating coupler," IEEE Photonics Technol. Lett. **22**(19), 1461–1463 (2010).
34. G. Maire, L. Vivien, G. Sattler, *et al.*, "High efficiency silicon nitride surface grating couplers," Opt. Express **16**(1), 328–333 (2008).
35. H. Zhang, C. Li, X. Tu, *et al.*, "High efficiency silicon nitride grating coupler," Appl. Phys. A **115**(1), 79–82 (2014).
36. M. J. Shaw, J. Guo, G. A. Vawter, *et al.*, "Fabrication techniques for low-loss silicon nitride waveguides," in *Micromachining Technology for Micro-Optics and Nano-Optics III*, vol. 5720 (SPIE, 2005), pp. 109–118.
37. S. Kim, D. A. Westly, B. J. Roxworthy, *et al.*, "Photonic waveguide to free-space gaussian beam extreme mode converter," Light: Sci. Appl. **7**(1), 72 (2018).
38. R. Marchetti, C. Lacava, A. Khokhar, *et al.*, "High-efficiency grating-couplers: demonstration of a new design strategy," Sci. Rep. **7**(1), 16670 (2017).
39. Q. Liu, Z. Shi, G. Zhu, *et al.*, "Freestanding gan grating couplers at visible wavelengths," J. Opt. **17**(4), 045607 (2015).
40. Lumerical Inc., "FDTD: 3D Electromagnetic Simulator: 2020 R2.4, version: 8.24.2502," (2020). https://www.lumerical.com/.
41. M. A. Talukder, C. R. Menyuk, and Y. Kostov, "Distinguishing between whole cells and cell debris using surface plasmon coupled emission," Biomed. Opt. Express **9**(4), 1977–1991 (2018).
42. W. Choi, C. Fang-Yen, K. Badizadegan, *et al.*, "Tomographic phase microscopy," Nat. Methods **4**(9), 717–719 (2007).
43. H. Li, W. Zhou, M. Zhang, *et al.*, "Large-area binary blazed grating coupler between nanophotonic waveguide and LED," The Sci. World J. **2014**, 1–6 (2014).
44. S. Romero-García, F. Merget, F. Zhong, *et al.*, "Silicon nitride CMOS-compatible platform for integrated photonics applications at visible wavelengths," Opt. Express **21**(12), 14036–14046 (2013).
45. J. Witzens, A. Scherer, G. Pickrell, *et al.*, "Monolithic integration of vertical-cavity surface-emitting lasers with in-plane waveguides," Appl. Phys. Lett. **86**(10), 101105 (2005).
46. S. De, K. Moessner, N. Gligoric, *et al.*, "SmartTags: IoT product passport for circular economy based on printed sensors and unique item-level identifiers," Sensors **19**(3), 586 (2019).
47. O. M. Solyman, O. Hamdy, S. A. Abdelkawi, *et al.*, "Investigating the light emitting diode (LED) flashlight characteristics of a sample of smartphones for its safety in indirect retinal photography," The Pan Afr. Med. J. **43**, 1 (2022).
48. L. Cheng, S. Mao, Z. Li, *et al.*, "Grating couplers on silicon photonics: Design principles, emerging trends and practical issues," Micromachines **11**(7), 666 (2020).
49. Z. Zhang, B. Huang, Z. Zhang, *et al.*, "Highly efficient vertical fiber interfacing grating coupler with bilayer anti-reflection cladding and backside metal mirror," Opt. & Laser Technol. **90**, 136–143 (2017).
50. S. Romero-García, F. Merget, F. Zhong, *et al.*, "Visible wavelength silicon nitride focusing grating coupler with AlCu/TiN reflector," Opt. Lett. **38**(14), 2521–2523 (2013).
51. J. D. Wong-Campos, J. Porto, and A. E. Cohen, "Which way does stimulated emission go?" J. Phys. Chem. A **125**(50), 10667–10676 (2021).
52. R. G. Geethu Mani and M. Basheer Ahamed, "Energy transfer studies for the liquid and solid state materials of Rhodamine B and Styryl 7 Dye," Optik **154**, 566–575 (2018).